Coherent Josephson Qubit Suitable for Scalable Quantum Integrated Circuits

R. Barends, J. Kelly, A. Megrant, D. Sank, E. Jeffrey, Y. Chen, Y. Yin,* B. Chiaro, J. Mutus, C. Neill, P. O'Malley, P. Roushan, J. Wenner, T. C. White, A. N. Cleland, and John M. Martinis

Department of Physics, University of California, Santa Barbara, California 93106, USA

(Received 5 April 2013; published 22 August 2013)

We demonstrate a planar, tunable superconducting qubit with energy relaxation times up to 44 μs. This is achieved by using a geometry designed to both minimize radiative loss and reduce coupling to materials-related defects. At these levels of coherence, we find a fine structure in the qubit energy lifetime as a function of frequency, indicating the presence of a sparse population of incoherent, weakly coupled two-level defects. We elucidate this defect physics by experimentally varying the geometry and by a model analysis. Our "Xmon" qubit combines facile fabrication, straightforward connectivity, fast control, and long coherence, opening a viable route to constructing a chip-based quantum computer.

DOI: 10.1103/PhysRevLett.111.080502 PACS numbers: 03.67.Lx, 03.65.Yz, 85.25.Cp

One of the outstanding challenges in building a quantum computer is to balance coherence, connectivity, and control in the qubits. Superconductivity provides an appealing platform because it allows for scalability: the conduction electrons condense into a macroscopic quantum state, and large quantum integrated circuits can be made with many elements having individual control lines. However, quantum coherence in superconducting circuits has proven to be very delicate, as it is easily disturbed by material defects, electron system excitations, and radiative coupling to external wiring [1–8]. To minimize these and other effects, many groups have recently begun embedding qubits in three-dimensional superconducting cavities. These 3D qubits show high coherence, with energy relaxation times in 3D transmon qubits between 30 and 140 μs [9,10].

Here, we demonstrate a new design for a fully planar superconducting qubit, based on the planar transmon [11,12], with energy coherence times in excess of 40 μs. Our approach balances coherence, connectivity, as well as fast control. The qubits are frequency tunable, which allows the implementation of fast two-qubit gates: a CONTROLLED-Z gate [13–15] can then be implemented with high fidelity in 25 ns [16]. With the coherence time exceeding single- and two-qubit gate times by 3 orders of magnitude, we believe that our device provides a key ingredient for implementing a surface code quantum computer [17].

We also identify an incoherent decoherence mechanism, arising from a sparse bath of weakly coupled defects. This incoherent regime is made accessible by the long coherence of our qubits. We explore this physics by visualizing these defects in the measured quantum time-resolved spectroscopy, by varying the qubit geometry, and by a model analysis. These defects give rise to frequency-dependent variations in the lifetime; our results may also explain the variations observed in lifetimes of 3D transmon qubits.

Our device is shown in Fig. 1(a), formed by patterning the Al metal (light areas) and exposing the sapphire substrate (dark areas). The qubit is the cross-shaped device. We design the qubit with high-quality coplanar waveguide capacitors, motivated by the recent advances with superconducting resonators, yielding a modular design with straightforward connectivity. Its four arms connect to separate elements, each having a different function: a coplanar waveguide resonator for readout on the top, a quantum bus resonator on the right to mediate coupling to other qubits, XY control on the left to excite the qubit state, and Z control on the bottom to tune the qubit frequency. The cross is the qubit capacitor, which connects at the bottom to the tunable Josephson junction, formed by the rectangular

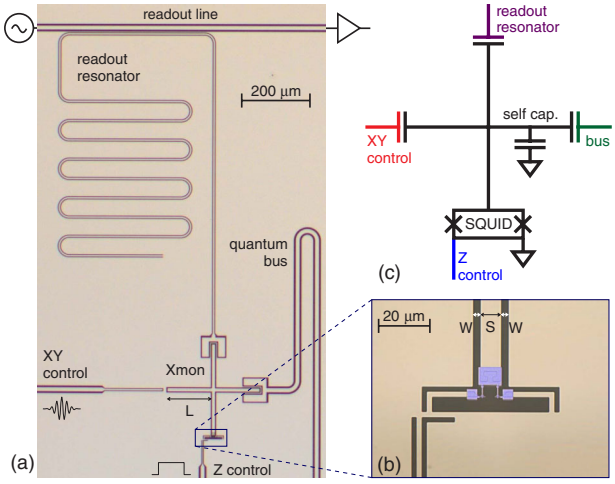

FIG. 1 (color online). (a) Optical micrograph of the planar Xmon qubit, formed by the Al superconducting film (light) and the exposed sapphire substrate (dark). The qubit is capacitively coupled to a quarter wave readout resonator (top), a quantum bus resonator (right), and an XY control line (left), and inductively coupled to a Z control line (bottom). The Xmon arm length is L. (b) The inset shows the shadow evaporated Al junction layer in false color (blue regions). The junction size is 0.30×0.20 μm^2. The capacitor central linewidth is S, and the gap width is W. (c) The electrical circuit of the qubit.

ring-shaped superconducting quantum interference device (SQUID); see Fig. 1(b). The rectangular ring is intersected by two identically sized Al tunnel junctions [blue regions in Fig. 1(b)]. The electrical circuit is equivalent to that of a grounded transmon [11], with the capacitor in parallel with the tunable junction [Fig. 1(c)]. In a clear departure from the traditional floating transmon with an interdigitated capacitor [12], we chose to form the qubit capacitor by intersecting two coplanar waveguide lines.

In prior work, we showed that highly coherent coplanar waveguide resonators can be fabricated, having quality factors of about 1.5×10^6 at the single photon occupation level. These resonators were made from molecular beam epitaxy (MBE) Al on oxygen-cleaned sapphire [18]. This shows that a straightforward path to high coherence comes from a combination of (I) MBE Al as high-quality material, (II) coplanar waveguides having low radiative loss, and (III) embedding in a ground plane. We therefore embed the qubit in an uninterrupted ground plane, with thin Al lines at the capacitor ends tying the ground planes together; this suppresses parasitic slot line modes in the control lines and resonators as well.

Connectivity is accomplished by coupling each of the qubit's arms to a distinct element with specific functionality. Three of the connections are easily made with a coupling capacitor, as the qubit is connected to ground. An advantage of this approach is that each coupling can be individually tuned and optimized. To this end, we have also separated out qubit control. The XY control drive line is connected with a coupling $C_c = 60$ aF, which allows us to excite the qubit state in 10 ns but hardly affects coherence, with an estimated T_1 of 0.3 ms. The Z control also combines speed and coherence. The drive line is galvanically connected to the SQUID to allow for a large inductive coupling with a mutual inductance of $M = 2.2$ pH. We are able to rapidly detune the qubit on the time scale of a nanosecond [19]. The measured parasitic coupling between the Z line and the qubit gives an estimated T_1 of ~30 ms [20].

We believe that the large increase in the qubit coherence relies critically on the *combination* of changes to the qubit design; implementing just one or two of these changes in isolation would not yield a significant improvement. With this experimental nature in mind, we name our qubit the "Xmon." While the cross-shaped qubit capacitor may emphasize this name, more arms can be added to allow for more connectivity.

We find a dramatic increase in Xmon energy coherence compared to the traditional planar transmon, measuring decay times up to $T_1 = 44$ μs; see Fig. 2(a). We find Ramsey and spin echo phase coherence times up to $T_2^* = 15$ μs and $T_2 = 20$ μs at the flux insensitive point, respectively [see Fig. 2(b)]; $T_1 = 18$ μs at this point. The dephasing envelopes follow an exponential decay, measured using tomography. The first pulse is $X_{\pi/2}$, followed by $X_{\pi/2}$, $X_{-\pi/2}$, $Y_{\pi/2}$, or $Y_{-\pi/2}$ (see the inset), producing fringes with different phases. The limit of $T_2 = 2T_1$ has not been reached [11], indicating additional dephasing. This, as well as dephasing away from the flux insensitive point, is presently under investigation.

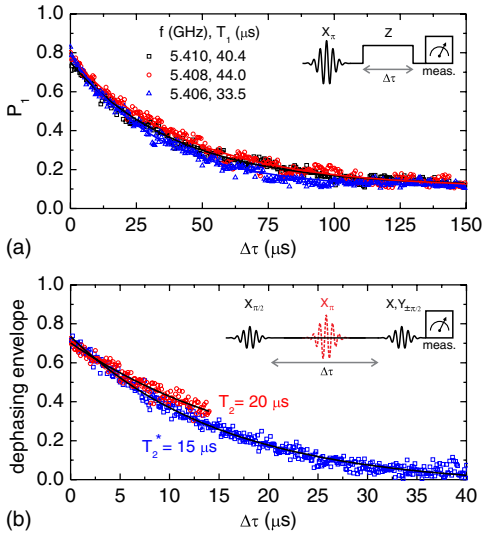

FIG. 2 (color online). (a) Qubit energy decay at three nearby frequencies ($S = W = 16$ μm [43]). The qubit frequency is adjusted by applying a rectangular pulse with length $\Delta\tau$ on the Z line. The pulse sequence is shown in the inset. (b) Ramsey T_2^* and spin echo T_2 dephasing envelopes at the flux insensitive point ($T_1 = 18$ μs), measured by phase tomography ($S = W = 24$ μm). The inset shows the pulse sequence; for the spin echo, we apply a refocusing pulse (dashed line). We apply four phases to the last pulse for phase tomography, to measure the decay envelope. Spin echo measurements are limited by electronics to 14 μs.

The qubits had ground to excited state transition frequencies around 6 GHz when unbiased, nonlinearities around 230 MHz, and a ratio of Josephson to charging energy $E_J/E_C \sim 95$. We employ a dispersive, high-power single-shot readout scheme with a 70%–85% fidelity [21]. The readout resonator frequencies used are 6.4–6.7 GHz, the loaded quality factor is $Q_l = 10^4$, and the resonator-qubit coupling strength is approximately 40 MHz. Measurements were done in a dilution refrigerator with a base temperature of 30 mK, with multistage infrared shielding [22]. Magnetic fields were reduced by room temperature and cryogenic magnetic shields, with nonmagnetic microwave connectors [23].

The results in Fig. 2 show that tunable superconducting qubits with a planar geometry can have T_1 values in excess of 40 μs. In fact, this T_1 corresponds to the MBE Al resonator quality factors [18], for which $T_1 = Q/\omega$ is also about 40 μs. The combination of long energy and phase coherence times compares well with previously reported values for planar superconducting Al qubits: for transmons $T_1 = 9.7$ μs and $T_2^* = 10$ μs [24], for charge qubits $T_1 = 200$ μs and $T_2^* = 0.07$ μs [25], for flux qubits $T_1 = 12$ μs and $T_2^* = 2.5$ μs [26], and for the fluxonium $T_1 = 10$ μs and $T_2^* = 2$ μs [27]. In fact, the Xmon approaches the long coherence found in 3D transmons [9,10]. Very recently, TiN planar devices have shown

long coherence [28,29], encouraging using Xmon geometries with this material.

We find that the energy relaxation depends on qubit frequency. As shown in Fig. 2(a), we find T_1 values from 34 to 44 μs in a 4 MHz band near 5.4 GHz. In order to elucidate this further, we performed a spectroscopic scan on the qubit, shown in Fig. 3(a). The qubit frequency displays the expected dependence on applied flux Φ [11], varying smoothly without visible splittings, indicating that strongly coupled defects, which manifest as avoided level crossings [1], are virtually absent. We then performed a quantum analogue of time-resolved spectroscopy (swap spectroscopy [30]), shown in Fig. 3(b). The pulse sequence is shown in Fig. 2(a). The probability of the excited state (color) is plotted for $\Delta\tau$ from 100 ns to 150 μs (logarithmic vertical scale) and qubit frequencies from 4 to 6 GHz. We find that the probability decays exponentially, but with a fine structure of variable energy relaxation and distinct peaks in the energy decay rate [Fig. 3(c)]. We do not observe any "chevron" interference patterns [30], where the quantum state coherently swaps back and forth, implying no defects interact coherently with the qubit. After cycling the temperature to 4.2 K, the fine structure is altered, but the overall image remains unchanged. We count approximately 30 regions with reduced coherence ($T_1 < 8$ μs) per GHz in Fig. 3(b).

We explored the dependence of the qubit coherence time on capacitor geometry, using six different designs; the width S of the central line, gap width W, and arm length L were varied, while the capacitance value [31] and junction parameters are kept the same. The parameters are listed in Table I;

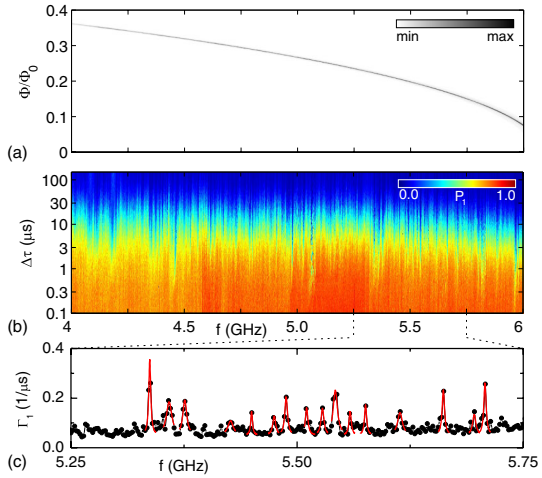

FIG. 3 (color online). (a) Qubit spectroscopy for a device with $S, W = 8, 8$ μm. A smooth curve is formed by the high transmission (gray line), measured on resonance with the readout resonator, which indicates when the qubit is excited. (b) Swap spectroscopy of the same qubit. The qubit is detuned from 4 to 6 GHz (step size 2 MHz), and the delay time is varied from 100 ns to 150 μs. See the inset of Fig. 2(a) for the pulse sequence. (c) Qubit relaxation rates, extracted from the data in (b). The peaks are fitted to Eq. (1) (solid lines).

see Ref. [19] for a micrograph. We find that the swap spectroscopy measurements of the different designs share the same characteristics as shown in Fig. 3(b): a fine structure with varying exponential decay. The energy relaxation times extracted from the measurements are shown in Fig. 4. The overall energy relaxation time increases with width: when changing S,W from $8,4$ μm to $16,8$ μm and $24,12$ μm, the T_1 improves from a band of values between 8 and 15 to 10 and 20, and 20 and 40 μs, respectively. Importantly, both the upper and lower bounds on T_1 increase. This is repeated in the qubits with S,W ranging from 8,8 to 16,16 and 24, 24 μm. The reduction of T_1 at frequencies approaching 6 GHz is due to Purcell decay into the readout resonator [32]. We emphasize that these T_1 values are obtained in multiqubit chips with control wiring.

The improvement of T_1 with increasing width is consistent with previous experiments on superconducting resonators [33,34]. Loss arises from the electric fields coupling to two-level systems with dipole moments [35], which reside predominantly in surface oxides and interfaces. This loss depends on the participation ratio, which depends on the electric field distribution [36]. Widening the capacitor reduces the surface participation, a natural explanation for the approximately linear increase in average T_1 with width in Fig. 4. On the other hand, the peaks in the decay rate are reminiscent of experiments with phase qubits [1], where localized features in the frequency dependence occur when the qubit couples strongly to two-level defects, often giving rise to splitting of the qubit frequency and the chevron-shaped signature of coherent swapping. However, the exponential decay in the Xmon qubit, with no signatures of swapping or splitting, suggests a different energy relaxation mechanism.

Here, we show how surface defects near the metal edges of the capacitor provide a natural explanation for the peaks in the energy decay. As indicated by the data, the key point is that loss arises from the qubit interacting with a sparse bath of incoherent, weakly coupled defects, giving rise to incoherent decay [37]. The sharp frequency dependence as well as the changes in fine structure when cycling to 4.2 K are consistent with defects. The absence of chevrons and qubit frequency splittings corresponds to incoherent interaction. The lower and upper bounds of T_1 increasing with capacitor dimension indicate that the defects reside in the capacitor.

We model a quantum system consisting of a qubit, with a frequency-independent loss rate $\Gamma_{1,Q}$ and pure dephasing rate $\Gamma_{\phi,Q}$, and a two-level defect with decoherence rate

TABLE I. Geometric parameters for the Xmon qubit capacitors as defined in Fig. 1 along with their frequencies. Groups of three qubits indicate that the devices are on the same chips.

S (μm)	8	16	24	8	16	24
W (μm)	4	8	12	8	16	24
L (μm)	130	130	130	165	165	165
$f_{10,\max}$ (GHz)	6.094	6.158	6.071	6.080	5.883	5.846
Nonlinearity (MHz)	224	228	222	220	225	223

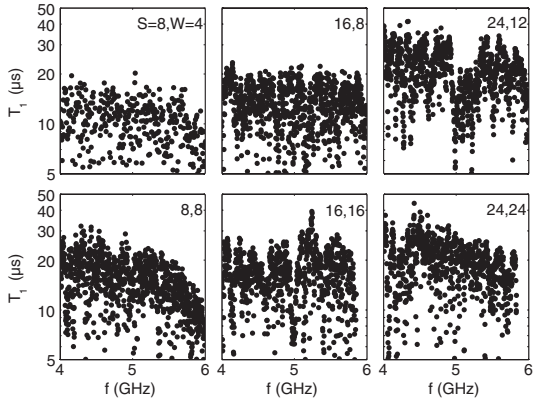

FIG. 4. Frequency dependence of T_1 for six qubits with different S and W (see Table I). The frequency step size is 5 MHz for S, $W = 8$, 4 μm and 2 MHz otherwise. See Ref. [19] for the corresponding decay rates.

$\Gamma_{1,D}$ and dephasing rate $\Gamma_{\phi,D}$ [19]; we assume Markovian decoherence. When $\Gamma_{1,D}$ exceeds the coupling strength g, coherent swapping vanishes and an incoherent, exponential decay appears. From a two-spin Hamiltonian [19], we derive the qubit energy relaxation rate Γ_1 (in the limit $\Gamma_{1,D} > g > \Gamma_{1,Q}$)

$$\Gamma_1 = \frac{2g^2\Gamma}{\Gamma^2 + \Delta^2} + \Gamma_{1,Q}, \tag{1}$$

with detuning Δ, and $\Gamma = \Gamma_{1,D}/2 + \Gamma_{\phi,D} + \Gamma_{1,Q}/2 + \Gamma_{\phi,Q}$. Hence, each uncorrelated defect adds a single Lorentzian to the energy decay rate. We can roughly estimate g for a surface defect with dipole moment $p \sim 1$ Debye at a distance x away from the metal edge. With the electric field given by $E = B/\sqrt{x}$ [38] and B from numerical simulations [39], we arrive at $g/2\pi \sim 0.1$ MHz ($g = pE$) for $x = 3$ nm. We apply our model to Fig. 3(c). The peaks in decay rate can be described by a set of Lorentzians, with $1/(\Gamma_{1,D}/2 + \Gamma_{\phi,D}) \sim 50$–$100$ ns, consistent with defect decay rates measured in similar systems [1,40] and with $g/2\pi \gtrsim 0.2$ MHz, agreeing with incoherent loss.

We can also estimate the number of individually resolvable defects using two-level system physics developed for junctions. The substrate-metal interface in our devices was thoroughly cleaned [18]; hence, we assume that the bulk of strongly coupled defects resides in the metal- and substrate-air interfaces, as they have the highest participation ratios [36]. The defect density for AlO_x in tunnel barriers has been established in measurements with phase qubits [1], with the distribution over dipole moment given by $\rho_0\sqrt{1 - p^2/p_{\max}^2}/p$, with $\rho_0 \approx 10^2/\mu\text{m}^3/\text{GHz}$, and the maximum dipole moment $p_{\max} = 6$ Debye. We take these numbers as representative and assume a 3 nm thick dielectric layer with defects [41]. The number of defects with coupling strength greater than $g_{\min}$ is then given by

$$N = \iint \rho_0 \frac{\sqrt{1 - p^2/p_{\max}^2}}{p} \Theta[p|E(\vec{r})| - g_{\min}] dp d\vec{r}, \tag{2}$$

with Θ the unit step function and $E(\vec{r})$ the electric field at position $\vec{r}$. Simulations using Eq. (2) as well as Monte Carlo simulations indicate $N \sim 30$–50/GHz, for $g_{\min}/2\pi \sim 0.2$ MHz; see Ref. [19]. We emphasize that the simulations connect $g_{\min}$ to N with values which are close to what is observed experimentally. The simulations also indicate that the bulk of strongly coupled defects reside within a $\sim$100 nm distance from the etched edges, where the electric fields are largest. In addition, the simulated qubit decay rate reproduces the experimentally observed features, showing both the peaks and background variation.

The good quantitative comparison between model and experiment gives compelling evidence that a sparse bath of incoherent defects plays a major role in loss in highly coherent qubits. Our results may also explain previously reported anomalous behavior in planar transmon qubits with long coherence, for which the T_1 has been reported to vary significantly between qubits, even on the same chip [24,42]. This is consistent with a sparse bath of incoherent defects limiting the coherence, as in Fig. 3.

In conclusion, we demonstrate energy coherence times exceeding 40 μs in tunable, planar superconducting qubits. We have achieved this using a geometry with low radiative dissipation and high-quality materials. At these high coherence levels, we identify a novel decoherence mechanism, loss from a sparse bath of incoherent defects, which is apparent in the swap spectroscopy. Our qubits combine long coherence, easy interconnectivity, and fast control, providing a key ingredient for the implementation of an on-chip surface code quantum computer.

We thank A. N. Korotkov for valuable discussions. This work was supported by the Rubicon program of the Netherlands Organisation for Scientific Research (NWO) and by the Office of the Director of National Intelligence (ODNI), Intelligence Advanced Research Projects Activity (IARPA), through the Army Research Office Grants No. W911NF-09-1-0375 and No. W911NF-10-1-0334. All statements of fact, opinion, or conclusions contained herein are those of the authors and should not be construed as representing the official views or policies of IARPA, the ODNI, or the U.S. Government. Devices were made at the UC Santa Barbara Nanofabrication Facility, a part of the NSF-funded National Nanotechnology Infrastructure Network, and at the NanoStructures Cleanroom Facility. R. Barends and J. Kelly contributed equally to this work.

*Present address: Department of Physics, Zhejiang University, Hangzhou 310027, China.

[1] J. M. Martinis, K. B. Cooper, R. McDermott, M. Steffen, M. Ansmann, K. D. Osborn, K. Cicak, S. Oh, D. P. Pappas, R. W. Simmonds, and C. C. Yu, Phys. Rev. Lett. **95**, 210503 (2005).
[2] A. Shnirman, G. Schön, I. Martin, and Yu. Makhlin, Phys. Rev. Lett. **94**, 127002 (2005).
[3] G. J. Grabovskij, T. Peichl, J. Lisenfeld, G. Weiss, and A. V. Ustinov, Science **338**, 232 (2012).

[4] J. Wenner, Y. Yin, E. Lucero, R. Barends, Y. Chen, B. Chiaro, J. Kelly, M. Lenander, M. Mariantoni, A. Megrant, C. Neill, P. J. J. O'Malley, D. Sank, A. Vainsencher, H. Wang, T. C. White, A. N. Cleland, and J. M. Martinis, Phys. Rev. Lett. **110**, 150502 (2013).

[5] G. Catelani, S. E. Nigg, S. M. Girvin, R. J. Schoelkopf, and L. I. Glazman, Phys. Rev. B **86**, 184514 (2012).

[6] D. Ristè, C. C. Bultink, M. J. Tiggelman, R. N. Schouten, K. W. Lehnert, and L. DiCarlo, Nat. Commun. **4**, 1913 (2013).

[7] M. D. Shaw, R. M. Lutchyn, P. Delsing, and P. M. Echternach, Phys. Rev. B **78**, 024503 (2008).

[8] P. Lafarge, P. Joyez, D. Esteve, C. Urbina, and M. H. Devoret, Phys. Rev. Lett. **70**, 994 (1993).

[9] H. Paik, D. I. Schuster, L. S. Bishop, G. Kirchmair, G. Catelani, A. P. Sears, B. R. Johnson, M. J. Reagor, L. Frunzio, L. I. Glazman, S. M. Girvin, M. H. Devoret, and R. J. Schoelkopf, Phys. Rev. Lett. **107**, 240501 (2011),

[10] C. Rigetti, J. M. Gambetta, S. Poletto, B. L. T. Plourde, J. M. Chow, A. D. Córcoles, J. A. Smolin, S. T. Merkel, J. R. Rozen, G. A. Keefe, M. B. Rothwell, M. B. Ketchen, and M. Steffen, Phys. Rev. B **86**, 100506 (2012).

[11] J. Koch, T. M. Yu, J. Gambetta, A. A. Houck, D. I. Schuster, J. Majer, A. Blais, M. H. Devoret, S. M. Girvin, and R. J. Schoelkopf, Phys. Rev. A **76**, 042319 (2007).

[12] A. A. Houck, D. I. Schuster, J. M. Gambetta, J. A. Schreier, B. R. Johnson, J. M. Chow, L. Frunzio, J. Majer, M. H. Devoret, S. M. Girvin, and R. J. Schoelkopf, Nature (London) **449**, 328 (2007).

[13] F. W. Strauch, P. R. Johnson, A. J. Dragt, C. J. Lobb, J. R. Anderson, and F. C. Wellstood, Phys. Rev. Lett. **91**, 167005 (2003).

[14] L. DiCarlo, J. M. Chow, J. M. Gambetta, L. S. Bishop, B. R. Johnson, D. I. Schuster, J. Majer, A. Blais, L. Frunzio, S. M. Girvin, and R. J. Schoelkopf, Nature (London) **460**, 240 (2009).

[15] M. Mariantoni, H. Wang, T. Yamamoto, M. Neeley, R. C. Bialczak, Y. Chen, M. Lenander, E. Lucero, A. D. O'Connell, D. Sank, M. Weides, J. Wenner, Y. Yin, J. Zhao, A. N. Korotkov, A. N. Cleland, and J. M. Martinis, Science **334**, 61 (2011).

[16] J. Ghosh, A. Galiautdinov, Z. Zhou, A. N. Korotkov, J. M. Martinis, and M. R. Geller, Phys. Rev. A **87**, 022309 (2013).

[17] A. G. Fowler, M. Mariantoni, J. M. Martinis, and A. N. Cleland, Phys. Rev. A **86**, 032324 (2012).

[18] A. Megrant, C. Neill, R. Barends, B. Chiaro, Y. Chen, L. Feigl, J. Kelly, E. Lucero, M. Mariantoni, P. J. J. O'Malley, D. Sank, A. Vainsencher, J. Wenner, T. C. White, Y. Yin, J. Zhao, C. J. Palmstrøm, J. M. Martinis, and A. N. Cleland, Appl. Phys. Lett. **100**, 113510 (2012).

[19] See Supplemental Material at http://link.aps.org/supplemental/10.1103/PhysRevLett.111.080502 for a further description of the fabrication, devices, Z-control, and simulation results.

[20] We measure the effective inductive coupling between the qubit and inductive drive line [11] to be $M' = 0.1$ pH.

[21] M. D. Reed, L. DiCarlo, B. R. Johnson, L. Sun, D. I. Schuster, L. Frunzio, and R. J. Schoelkopf, Phys. Rev. Lett. **105**, 173601 (2010).

[22] R. Barends, J. Wenner, M. Lenander, Y. Chen, R. C. Bialczak, J. Kelly, E. Lucero, P. O'Malley, M. Mariantoni, D. Sank, H. Wang, T. C. White, Y. Yin, J. Zhao, A. N. Cleland, J. M. Martinis, and J. J. A. Baselmans, Appl. Phys. Lett. **99**, 113507 (2011).

[23] EZ Form Cable Corporation, Hamden, CT 06517, USA.

[24] J. M. Chow, J. M. Gambetta, A. D. Corcoles, S. T. Merkel, J. A. Smolin, C. Rigetti, S. Poletto, G. A. Keefe, M. B. Rothwell, J. R. Rozen, M. B. Ketchen, and M. Steffen, Phys. Rev. Lett. **109**, 060501 (2012).

[25] Z. Kim, B. Suri, V. Zaretskey, S. Novikov, K. D. Osborn, A. Mizel, F. C. Wellstood, and B. S. Palmer, Phys. Rev. Lett. **106**, 120501 (2011).

[26] J. Bylander, S. Gustavsson, F. Yan, F. Yoshihara, K. Harrabi, G. Fitch, D. G. Cory, Y. Nakamura, J.-S. Tsai, and W. D. Oliver, Nat. Phys. **7**, 565 (2011).

[27] V. E. Manucharyan, N. A. Masluk, A. Kamal, J. Koch, L. I. Glazman, and M. H. Devoret, Phys. Rev. B **85**, 024521 (2012).

[28] J. Chang, M. R. Vissers, A. D. Corcoles, M. Sandberg, J. Gao, D. W. Abraham, J. M. Chow, J. M. Gambetta, M. B. Rothwell, G. A. Keefe, M. Steffen, and D. P. Pappas, Appl. Phys. Lett. **103**, 012602 (2013).

[29] J. M. Sage, V. Bolkhovsky, W. D. Oliver, B. Turek, and P. B. Welander, J. Appl. Phys. **109**, 063915 (2011).

[30] K. B. Cooper, M. Steffen, R. McDermott, R. W. Simmonds, S. Oh, D. A. Hite, D. P. Pappas, and J. M. Martinis, Phys. Rev. Lett. **93**, 180401 (2004).

[31] The Xmon capacitance is closely approximated by the coplanar waveguide formula $C = 8L(\epsilon_0 + \epsilon_{\rm sub})K(k)/K(\sqrt{1-k^2})$, with ϵ_0 the vacuum permittivity, $\epsilon_{\rm sub}$ the substrate permittivity, $k = S/(S+2W)$, and K the complete elliptic integral.

[32] A. A. Houck, J. A. Schreier, B. R. Johnson, J. M. Chow, J. Koch, J. M. Gambetta, D. I. Schuster, L. Frunzio, M. H. Devoret, S. M. Girvin, and R. J. Schoelkopf, Phys. Rev. Lett. **101**, 080502 (2008).

[33] R. Barends, N. Vercruyssen, A. Endo, P. J. de Visser, T. Zijlstra, T. M. Klapwijk, P. Diener, S. J. C. Yates, and J. J. A. Baselmans, Appl. Phys. Lett. **97**, 023508 (2010).

[34] J. Gao, M. Daal, A. Vayonakis, S. Kumar, J. Zmuidzinas, B. Sadoulet, B. A. Mazin, P. K. Day, and H. G. Leduc, Appl. Phys. Lett. **92**, 152505 (2008).

[35] W. A. Phillips, Rep. Prog. Phys. **50**, 1657 (1987).

[36] J. Wenner, R. Barends, R. C. Bialczak, Yu. Chen, J. Kelly, E. Lucero, M. Mariantoni, A. Megrant, P. J. J. O'Malley, D. Sank, A. Vainsencher, H. Wang, T. C. White, Y. Yin, J. Zhao, A. N. Cleland, and J. M. Martinis, Appl. Phys. Lett. **99**, 113513 (2011).

[37] We define incoherent defects as having a decay rate exceeding the coupling strength and interacting incoherently with the qubit.

[38] J. D. Jackson, *Classical Electrodynamics* (Wiley, Hoboken, NJ, 1999), 3rd ed.

[39] For the $S = 8$, $W = 8$ geometry, we find for the electric field away from the metal edge in the plane of the substrate surface $E = B/\sqrt{x}$, with $B = 2$ mV$/\sqrt{\rm m}$.

[40] Y. Shalibo, Y. Rofe, D. Shwa, F. Zeides, M. Neeley, J. M. Martinis, and N. Katz, Phys. Rev. Lett. **105**, 177001 (2010).

[41] Using a thickness of 2 nm instead of 3 nm for the dielectric layer does not significantly affect the outcome.

[42] M. Sandberg, M. R. Vissers, T. Ohki, J. Gao, J. Aumentado, M. Weides, and D. P. Pappas, Appl. Phys. Lett. **102**, 072601 (2013).

[43] The data in Fig. 2 were taken in a different cooldown from the data in Fig. 3.